ROTOR DYNAMICS MODELING USING COUPLED MULTIBODY DYNAMICS AND A GPU-ACCELERATED VORTEX PARTICLE SOLVER

Navarajah Subramaniam
Research Associate

Muhammed Kürşat Yurt
Research Associate

İlkay Yavrucuk
Professor

Institute for Rotorcraft and Vertical Flight
Technical University of Munich
Munich, Germany

ABSTRACT

This paper presents a rotor dynamics modeling framework developed to investigate the behavior of an experimental rotor system. The framework integrates two in-house solvers: a Multibody Dynamics code and a GPU-accelerated vortex particle method, enabling efficient and accurate simulation of coupled aeromechanical systems. The multibody solver utilizes a rigid-body core formulation and employs blade element theory, along with airfoil lookup tables, to compute aerodynamic loads. The vortex particle wake model incorporates the Fast Multipole Method for computational efficiency. The viscous diffusion is simulated using Particle Strength Exchange and Core Spreading techniques. Simulation predictions show good agreement with UH-60 experimental data. The resulting framework provides a fast, accurate, and scalable tool for mid-fidelity rotorcraft wake simulations.

NOTATION

R	Rotor radius, m
u	Velocity, m/s
x	Position, m
C_T	Rotor thrust coefficient
C_P	Rotor power coefficient
C_l	Airfoil section lift coefficient
C_d	Airfoil section drag coefficient
c_{root}	Blade root chord length, m
c_{tip}	Blade root tip length, m
μ	Advance ratio
σ	Rotor solidity
ω	Vorticity, s^{-1}
∇	Gradient operator
α	Particle strength
$\tilde{\cdot}$	Filtered quantity
$\vec{\cdot}$	Vectorial quantity

INTRODUCTION

The unique demands of rotorcraft aeromechanics analysis, which require interdisciplinary models incorporating geometry, structure, dynamics, and aerodynamics, have been the driving force behind the development of comprehensive analysis tools. As rotorcraft configurations grow more advanced, their nonlinear and interconnected dynamic behavior necessitates the use of Multibody Dynamics (MBD) codes, integrated with various aerodynamic models. Advances in high-performance computing have enabled the application of Computational Fluid Dynamics (CFD) as an aerodynamic solver. However, despite its accuracy, CFD-MBD coupling remains limited as demonstrated in Ref. 1–3 due to the high computational cost and numerical diffusion inherent in conventional grid-based CFD methods.

Low-fidelity aerodynamic models, such as dynamic inflow, can effectively estimate induced flow, offering advantages in speed and computational efficiency. However, they fail to capture unsteady aerodynamic phenomena in which fluid rotation or simply vorticity plays a significant role. For instance, inaccuracies can arise when a tip vortex generated by one rotor blade moves near another blade. When the advance ratio μ is below 0.2, it becomes especially important for rotor wake models to accurately represent the dynamics of trailing and shed vortices, as strong blade–vortex interactions are common in this low-speed flight regime, as indicated in Ref. 4. Alvarez and Ning showed in Ref. 5 that in multirotor aerodynamic interactions, the accentuated induced upwash between the rotors is the main contributor to the drop in blade loading during rotor-on-rotor interaction.

In such cases, accurate modeling of wake interactions becomes critical, making mid-fidelity aerodynamic solvers such as the Lattice Boltzmann Method (LBM) and free-wake methods compelling alternatives. LBM solves the Lattice Boltzmann equation, which is a special discretized form of the Boltzmann equation. It resolves using particle distribution functions, rather than macroscopic quantities like velocity or density. The main disadvantages of the LBM are its sensitivity to grid resolution and relaxation parameters. Unlike grid-based approaches, freewake methods are Lagrangian and mesh-free, allowing the resolution of vortex structures over long distances without the numerical dissipation issues that plague Eulerian approaches. Traditional free wake solvers use vortex filaments to model wakes but face challenges in capturing near-wake distortions, vortex core growth, and wake mixing.

The Viscous Vortex Particle Method (VVPM) addresses these limitations by discretizing wake vorticity into particles rather than filaments, providing greater flexibility in modeling complex wake interactions. With sufficient particle resolution, VVPM can accurately capture both radial and azimuthal inflow variations, offering a level of fidelity beyond simplified filament methods while remaining significantly more computationally efficient than full CFD, as demonstrated in Ref. 6. The open-source code DUST in Ref. 7 has successfully implemented an MBD-VVPM coupling. Several studies from Ref. 8–10 report simulation runtimes ranging from hours to days, reflecting a significant bottleneck to broader adoption. These investigations consistently highlight the urgent need for faster computational turnaround to support practical design and analysis workflows.

This paper presents an enhanced rotor dynamics modeling capability, enabled by a newly developed in-house GPU-accelerated VVPM solver, VORTEX, introduced in Ref. 11, and coupled with the in-house MBD solver, ARCS, previously used by Reiser in Ref. 12 to investigate coaxial rotors coupled with an in-house LBM solver. Predictions from the coupled aeromechanics solver, including thrust and power, are compared with experimental data from the literature to demonstrate the framework's ability to accurately model rotor and wake dynamics.

METHODOLOGY

Viscous Vortex Particle Method (VVPM)

The Navier-Stokes equations describe the velocity field around the rotor, assuming the flow is incompressible. In its vorticity-velocity form, it can be written as:

$$\frac{\partial\vec{\omega}}{\partial t}+(\vec{u}\cdot\nabla)\vec{\omega}-(\vec{\omega}\cdot\nabla)\vec{u}=\nu\nabla^2\vec{\omega} \tag{1}$$

where $\vec{\omega}=\nabla\times\vec{u}$ is vorticity. The vorticity field can be approximated with N points in space that are represented by vortex particles:

$$\vec{\omega}(\vec{x},t)\approx\sum_{i}^{N}\delta(\vec{x}-\vec{x}_i(t))\vec{\alpha}_i(t) \tag{2}$$

Here, $\delta()$ denotes the Dirac delta function, which introduces singularities into the vorticity field. The vector $\vec{\alpha}$ represents the vorticity carried by each particle. To avoid these singularities in numerical simulations, a smoothing filter function $\zeta_\sigma()$ is applied, where σ is the filter width. Several filter functions have been proposed in Ref. 13; in this study, a Gaussian filter is used. The filtered Navier-Stokes equation in material derivative form is given as:

$$\frac{D\tilde{\vec{\omega}}}{Dt}=(\tilde{\vec{\omega}}\cdot\nabla)\tilde{\vec{u}}+\nu\nabla^2\tilde{\vec{\omega}}-\vec{T} \tag{3}$$

where $\tilde{\cdot}$ is the filtered quantity, and $\vec{T}$ represents the truncation error between the resolved and unresolved quantities due to the filtering process from Ref. 9. A turbulent viscosity model is used in this work to approximate this truncation error by modeling the loss of enstrophy transferred to the small scales, similar to Ref. 10:

$$\vec{T}=-\nabla\cdot(\nu_t(\nabla\otimes\tilde{\vec{\omega}})+(\nabla\otimes\tilde{\vec{\omega}})^t) \tag{4}$$

Hence, the LES-filtered vorticity equation becomes:

$$\frac{D\tilde{\vec{\omega}}}{Dt}=(\tilde{\vec{\omega}}\cdot\nabla)\tilde{\vec{u}}+\nabla\cdot\left((\nu+\nu_t)\left(\nabla\otimes\tilde{\vec{\omega}}\right)\right), \tag{5}$$

where ν_t is turbulent viscosity. While there are a variety of turbulent viscosity models available, shown in Ref. 14–16, in the current work, the Vreman model from Ref. 16 is implemented

$$\nu_t=c\sqrt{\frac{B_\beta}{\beta_{11}+\beta_{22}+\beta_{33}}}, \tag{6}$$

where $B_\beta=\beta_{11}\beta_{22}-\beta_{12}^2+\beta_{11}\beta_{33}-\beta_{13}^2+\beta_{22}\beta_{33}-\beta_{23}^2$, and $\beta=\left(\nabla^t\otimes\tilde{\vec{u}}\right)\left(\nabla\otimes\tilde{\vec{u}}\right)$. The modeling coefficient c in eq. (6), dynamically adjusted using the procedure described by Valentin in Ref. 10. The velocity field induced by the particles can be approximated using the Biot-Savart law:

$$\tilde{\vec{u}}(\vec{x_i},t)=-\sum_j\frac{g(\rho_{ij})}{4\pi r_{ij}^3}\vec{r}_{ij}\times\vec{\alpha}_j \tag{7}$$

where,

$$g(\rho)=\text{erf}\left(\frac{\rho}{\sqrt{2}}\right)-\frac{2\rho}{\sqrt{2\pi}}e^{\rho^2/2} \tag{8}$$

for the Gaussian filter.

The time evaluation of the vortex particles follows the reformulated formulation in Ref. 17.

ARCS-VORTEX Coupling

An in-house Multibody Dynamics Code, ARCS, developed at the Institute for Rotorcraft and Vertical Flight, is used for rotor blade dynamics Ref. 12. The aerodynamics of the blades are modeled with the Blade Element Method in ARCS. The provided inflow data and calculated blade dynamics are used for calculating the local angle of attack and Mach number, then using 2D airfoil tables, the aerodynamic coefficients are obtained, such as $C_l(\alpha, M), C_d(\alpha, M)$. The obtained lift is converted to bound circulation using the Kutta–Joukowski theorem described in Ref. 18.

$$L' = \rho V \Gamma \tag{9}$$

The calculated bound circulation and its location are passed to the particle solver, VORTEX. The new particles are created using the bound circulation as a vorticity source,

$$\gamma_{\text{wake}} = -\frac{d\Gamma}{dt} + V_b \nabla \cdot \Gamma \tag{10}$$

where the first term is shed vorticity and the second term is trailed vorticity.

An inflow-bound circulation coupling is established in a tightly coupled manner between the solvers. The wake dynamic is solved by the VVPM solver, and the resulting induced inflow data is relayed back to ARCS. At every timestep, the solvers exchange the inflow and bound circulation data as shown in fig. 1.

All components, including the blades, are modeled as rigid bodies with specified inertial properties. A swash plate mechanism is not included in the model; instead, the pitch angle is directly defined at the blade root joint. Similarly, the rotor's angular velocity is prescribed at the rotor shaft.

The prediction of trimmed rotor forces demands long-duration wake simulations with fine time discretization. ARCS includes a built-in trim algorithm described in Ref. 19. For the VVPM simulation, the control variables obtained using Dynamic-Inflow are used to initialize the trim algorithm.

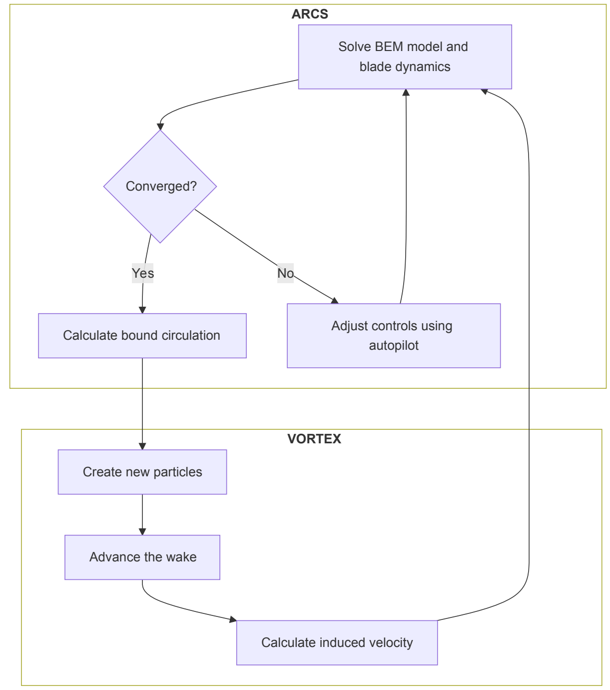

Figure 1: Flow chart indicating the exchange of information in the ARCS (Multibody) and VORTEX (VVPM) coupling framework.

RESULTS AND DISCUSSION

Reference Experiment & Rotor Model

The coupling framework is validated against experimental data from the UH-60 rotor tests conducted in the NASA Ames 80×120 ft wind tunnel. The isolated full-scale main rotor performance in this facility is documented by Shinoda et al. in Ref. 20. For the forward flight simulation case, a zero-degree shaft angle is taken and trimmed to have a constant flapping angle and specified blade loading during the rotation. The main rotor parameters and the simulation settings used for modeling are given in table 1.

Table 1: Experimental Rotor and Simulation Parameters

Parameter	**Value**
Rotor Parameters	
Number of blades N_b	4
Rotor radius R	8.179 m
Reference Blade chord c_{ref}	0.527 m
Nominal chord c_{root}, c_{tip}	0.54/046 m
Blade twist	$-18°$
Blade mass	116.53 kg
Rotational speed	25.13 rad s^{-1}
Rotor solidity	0.0826
Airfoil	SC1095/SC1094 R8
Simulation Parameters	
Time step	1° per azimuth
Shaft angle	0°
Number of blade elements	40
Air density	1.225 kg m^{-3}
Time Integration Order	4
Advance ratio μ	[0.0,0.2]
Blade loading C_T/σ	[0.06, 0.08, 0.09]

Hovering Rotor

Figure 2 compares the measured hover performance data from wind tunnel tests with simulation results using two different inflow calculation methods. The first method employs VORTEX, as described in the preceding section. The second method uses the Pitt–Peters dynamic inflow model from Ref. 21, a linear, unsteady formulation that captures the transient behavior of the induced flow based on the global rotor coefficients such as thrust, roll moment, and pitch moment. This model, however, does not account for wake progression. The simulation results show excellent agreement with the experimental data across all blade loading conditions for both approaches. The differences between the dynamic inflow model and VVPM in hover are minimal due to the limited interaction between the wake and rotor blades, since the wake predominantly convected downward under the influence of induced inflow in hover. Beyond a blade loading of $C_T/\sigma = 0.075$, VVPM predicts higher hover power compared to the dynamic inflow model, with the overprediction increasing significantly at higher blade loadings. Although no experimental data are available beyond $C_T/\sigma = 0.071$, the VVPM simulation appears to align more closely with the trend of the existing experimental data when extrapolated.

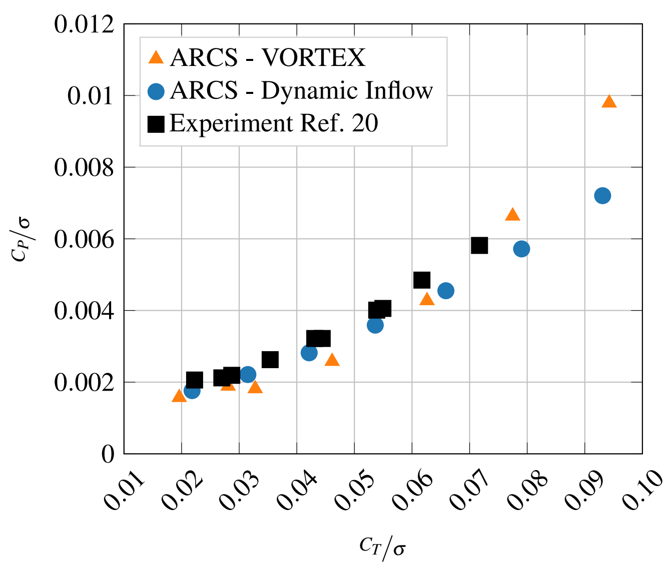

Figure 2: UH-60 rotor hover power comparison

Forward Flight

For the forward flight case, simulations were initially performed using the Pitt-Peters Dynamic Inflow within ARCS. The trimmed control angles obtained from the Dynamic Inflow simulation were used to initialize the VVPM simulations. This approach reduces computation time in the trimming algorithm. The corresponding results are illustrated in fig. 3. The simulation results using the Dynamic Inflow model closely match the experimental data, with a slight underprediction up until ($\mu \leq 0.15$) across all blade loadings.

Figure 4 presents the advance ratio sweep results and the corresponding power required at different blade loadings using ARCS-VORTEX. In general, the simulation data closely follow the experimental trends. As expected, for relatively low advance ratios ($\mu \leq 0.2$), the required power decreases with increasing μ for any given blade loading. This is primarily due to a reduction in induced power resulting from lower

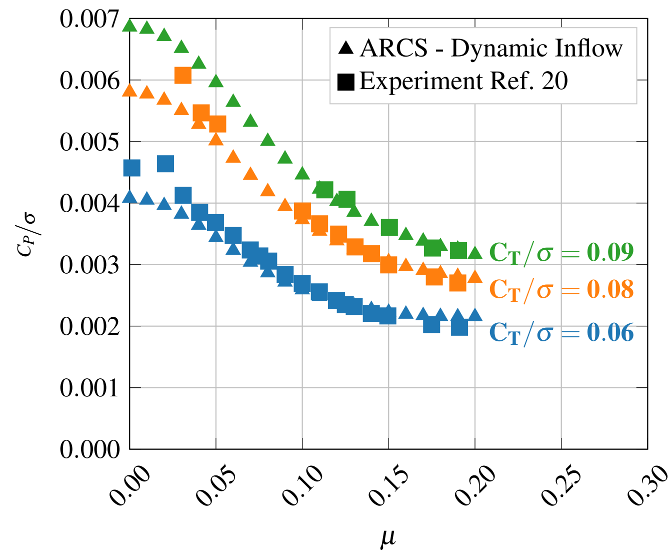

Figure 3: Measured and calculated rotor power using Dynamic Inflow vs. advance ratio for various thrust conditions

induced velocity. The profile power, which arises from rotor blade drag, increases more gradually within this interval. When comparing different blade loadings at a given forward flight speed, rotors with higher blade loading require more power due to the greater thrust demand. At $C_T/\sigma = 0.06$, the coupled framework overpredicts C_P/σ by maximum 17% for advance ratios $\mu \leq 0.08$ and underpredicts C_P/σ by maximum 21% for $\mu > 0.08$. A closer match between the simulation and experimental data is observed at higher blade loadings.

Although both the Dynamic-Inflow and VVPM predict global rotor values accurately, the advantage of the VVPM solver lies in its ability to more accurately capture local variation caused by the rotor wake. Consequently, differences between the two simulation frameworks are most likely to appear when analyzing local blade parameters. As shown in figs. 5 and 6, polar plots of induced inflow velocities and angle of attack are presented for three different advance ratios. These correspond to a thrust coefficient of $C_T/\sigma = 0.08$, which is one of the cases used for rotor power validation in the preceding section.

Simulations using the dynamic inflow model show a linear variation of inflow in the longitudinal direction across all advance ratios. The upwash is concentrated in the frontal region of the rotor disc, primarily between azimuth angles $\psi = 135°$ and $\psi = 225°$, with the highest values occurring near the blade tip. In contrast, the VVPM simulations reveal a more substantial upwash distributed over a broader frontal region. Notably, at the blade tip region, specifically around $\psi = 90°$ and $\psi = 270°$, the interaction and merging of tip vortices from multiple blades result in the formation of larger trailing vortices. The vortices are convected by self-induced and freestream velocity, which creates a skewed and contracted wake structure. This skewed wake naturally generates upwash in the frontal region and downwash in the aft portion of the rotor disc.

Another notable feature is the presence of root vortices, which predominantly interact near $\psi = 0°$ due to the freestream air-

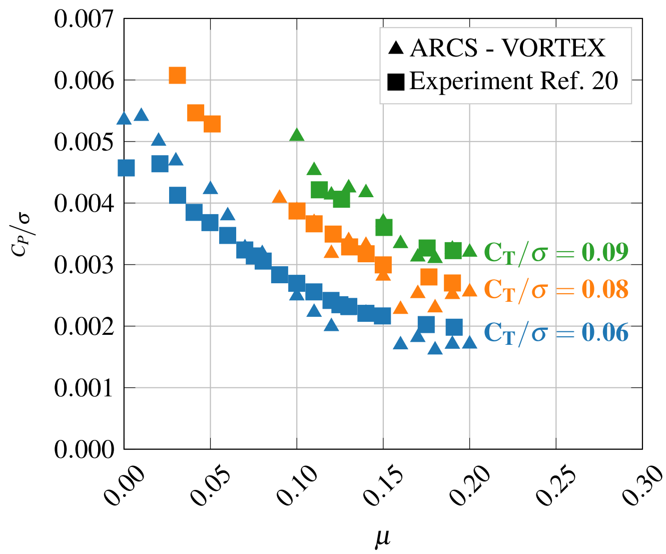

Figure 4: Measured and calculated rotor power using VVPM vs. advance ratio for various thrust conditions

flow, creating localized pockets of upwash. The effects of these root vortices are more clearly evident in the angle of attack polar plot shown in fig. 6. The small reverse-flow region near the blade root, indicated by dark blue areas representing highly negative angles of attack, is entirely absent in the VVPM simulations due to the influence of root vortices. These observations are consistent with the overall rotor wake structure shown in fig. 7, which is responsible for the observed undulations in the induced velocity. It should be noted that no blade root loss model was implemented, leading to much stronger root vortices than expected in all cases. The significantly higher vorticity at the blade root compared to the blade tip is considered nonphysical.

Another comparison can be made using predictions from the VVPM framework for two different blade loading conditions. As shown in fig. 8, polar plots of induced inflow velocities are presented for three different advance ratios at both low and high blade loading. At the same advance ratio, the rotor with higher blade loading exhibits a reduced influence from root vortices, resulting in a larger downwash region. As the forward flight speed increases, pockets of upwash expand in the rear section of the rotor disc.

CONCLUSIONS

This work presented a coupled aeromechanics framework that integrates a GPU-accelerated, viscous vortex particle method (VORTEX) with a multibody dynamics solver (ARCS). Based on comparison with experimental data from the UH-60 rotor test campaign, the following conclusions can be drawn:

1. The developed coupling between ARCS and VORTEX enables high-fidelity, time-accurate rotor wake modeling while maintaining computational efficiency through GPU parallelization.
2. The coupled solver accurately predicts global rotor performance metrics, such as thrust and power, in both hover and forward flight regimes, with good agreement across a wide range of advance ratios and blade loading conditions.
3. Unlike dynamic inflow models, the VVPM-based framework captures critical unsteady aerodynamic phenomena, including upwash, root vortex effects, and localized variations in induced velocity and angle of attack.
4. The simulation results demonstrate that high-resolution wake modeling can significantly enhance understanding of blade–vortex interactions and non-uniform inflow patterns, especially in low-speed and high blade loading flight conditions.

These results validate the capability of the coupled framework as a fast, scalable, and accurate tool for rotorcraft aeromechanics analysis, offering a promising alternative to conventional CFD–CSD approaches.

Author Contact:

Navarajah Subramaniam	navarajah.subramaniam@tum.de
Muhammed Kürşat Yurt	kursat.yurt@tum.de
Prof. Dr. phil. İlkay Yavrucuk	ilkay.yavrucuk@tum.de

REFERENCES

1. M. Potsdam, H. Yeo, and W. Johnson, "Rotor airloads prediction using loose aerodynamic/structural coupling," *Journal of Aircraft*, vol. 43, no. 3, pp. 732–742, 2006.

2. J. Lee, S. Oh, K. Yee, S. Kim, and D. Lee, "Loose coupling approach of CFD with a free-wake panel method for rotorcraft applications," *International Journal of Aeronautical and Space Sciences*, vol. 8, pp. 1–9, 2007.

3. F. Bensing, M. Keßler, and E. Krämer, "CFD-CSD-coupled simulations of helicopter rotors using an unstructured flow solver," in *High Performance Computing in Science and Engineering '10* (W. E. Nagel, D. B. Kröner, and M. M. Resch, eds.), (Berlin, Heidelberg), pp. 393–406, Springer Berlin Heidelberg, 2011.

4. W. Johnson, "A general free wake geometry calculation for wings and rotors," in *American Helicopter Society 51st Annual Forumm*, May 1995.

5. E. Alvarez and A. Ning, "Modeling multirotor aerodynamic interactions through the vortex particle method," in *AIAA Aviation 2019 Forum*, 06 2019.

6. C. He and J. Zhao, "Modeling rotor wake dynamics with viscous vortex particle method," *AIAA Journal*, vol. 47, no. 4, pp. 902–915, 2009.

7. M. Tugnoli, D. Montagnani, M. Syal, G. Droandi, and A. Zanotti, "Mid-fidelity approach to aerodynamic simulations of unconventional VTOL aircraft configurations," *Aerospace Science and Technology*, vol. 115, p. 106804, 2021.

8. M. Şenipek, *Investigation of Vortex Ring State for Multi-Rotor eVTOL Using Viscous Vortex Particle Method*. PhD thesis, Middle East Technical University, 2024.

9. E. J. Alvarez, *Reformulated Vortex Particle Method and Meshless Large Eddy Simulation of Multirotor Aircraft*. Phd thesis, Brigham Young University, 2002.

10. J. Valentin, *Multi-Fidelity Vortex Particles Coupling with Lifting Line and Eulerian Methods for 3D Viscous Aeronautical Simulations*. PhD thesis, Normandie Université, 2024.

11. M. K. Yurt, B. Bolgül, and I. Yavrucuk, "Meshless large eddy simulation of rotorcrafts using gpus," in *Proceedings of the Vertical Flight Society 81st Annual Forum and Technology Display*, p. 1–11, The Vertical Flight Society, May 2025.

12. A. Reiser and I. Yavrucuk, "Investigation of rotor interactional aerodynamics using the lattice boltzmann method," in *Proceedings of the Vertical Flight Society 80th Annual Forum*, p. 1–11, The Vertical Flight Society, May 2024.

13. G. S. Winckelmans, *Topics in vortex methods for the computation of three-and two-dimensional incompressible unsteady flows*. California Institute of Technology, 1989.

14. D. Kwak, W. C. Reynolds, and J. H. Ferziger, "Three-dimensional time dependent computation of turbulent flow," Contractor Report SU-TF-5, NASA-CR-166408, Stanford University, Thermosciences Division, Department of Mechanical Engineering, Stanford, California, May 1975. Prepared under NASA Grant NGR-05-020-622; reproduced by National Technical Information Service as NTIS 75N30477.

15. J. Smagorinsky, "General circulation experiments with the primitive equations: I. the basic experiment," *Monthly weather review*, vol. 91, no. 3, pp. 99–164, 1963.

16. A. Vreman, "An eddy-viscosity subgrid-scale model for turbulent shear flow: Algebraic theory and applications," *Physics of fluids*, vol. 16, no. 10, pp. 3670–3681, 2004.

17. E. J. Alvarez and A. Ning, "Reviving the vortex particle method: A stable formulation for meshless large eddy simulation," 2022.

18. J. D. Anderson, *Fundamentals of Aerodynamics*. New York, NY 10020: McGraw-Hill, 2011.

19. O. A. Bauchau, *Dymore User's Manual*. School of Aerospace Engineering, Georgia Institute of Technology, 2007.

20. P. M. Shinoda, H. Yeo, and T. R. Norman, "Rotor performance of a uh-60 rotor system in the nasa ames 80- by 120-foot wind tunnel," *Journal of the American Helicopter Society*, vol. 49, p. 401–413, Oct. 2004.

21. D. Pitt and D. Peters, "Theoretical prediction of dynamic-inflow derivatives," *Vertica*, vol. 5, 01 1981.

APPENDIX

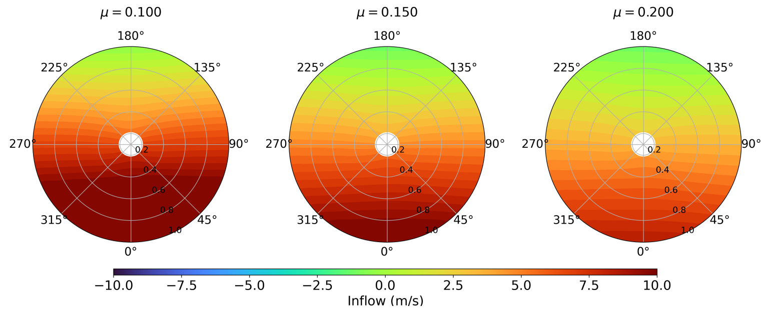

(a) Dynamic Inflow.

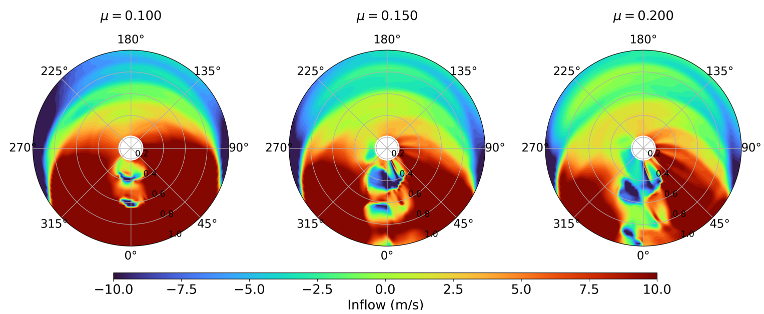

(b) Vortex Particle Method.

Figure 5: Contour plots of inflow velocity z component for $C_T/\sigma = 0.08$ using dynamic inflow and vortex particle wake.

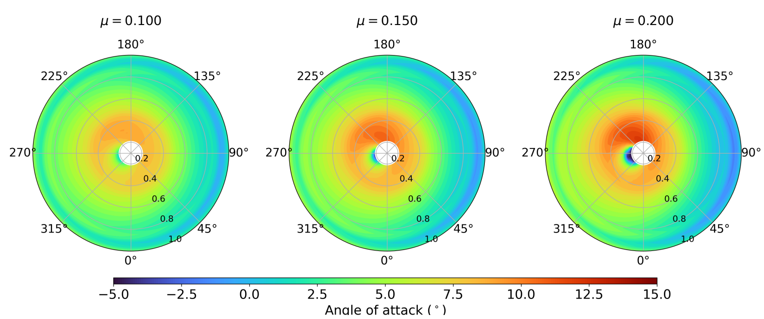

(a) Dynamic Inflow.

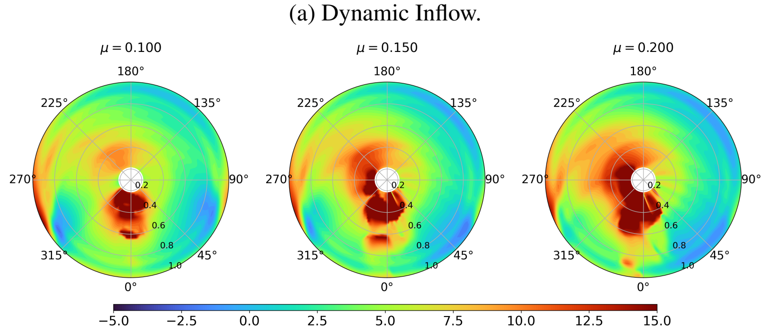

(b) Vortex Particle Method.

Figure 6: Contour plots of angle of attack for $C_T/\sigma = 0.08$ using dynamic inflow and vortex particle wake.

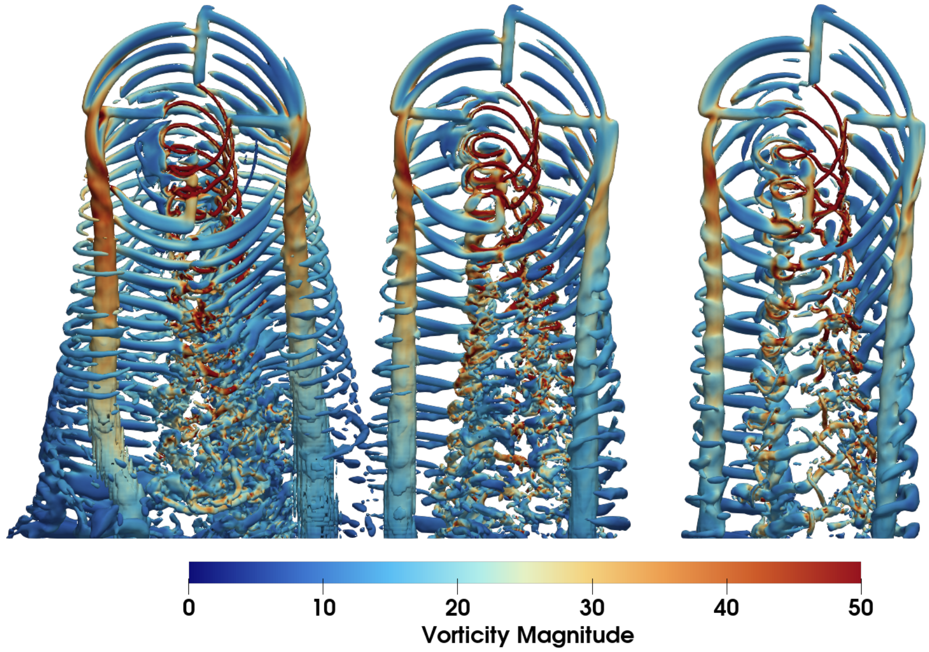

Figure 7: Isosurface of Q-Criterion magnitude of 10 colored by vorticity magnitude at $C_T/\sigma = 0.80$ at advance ratios $\mu = 0.10$ (left), $\mu = 0.15$ (middle), and $\mu = 0.20$ (right).

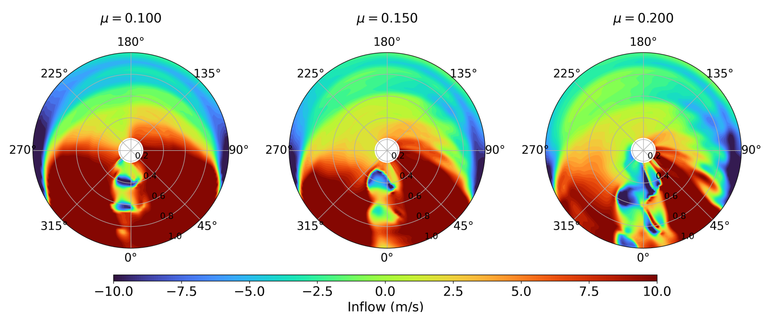

(a) $C_T/\sigma = 0.06$.

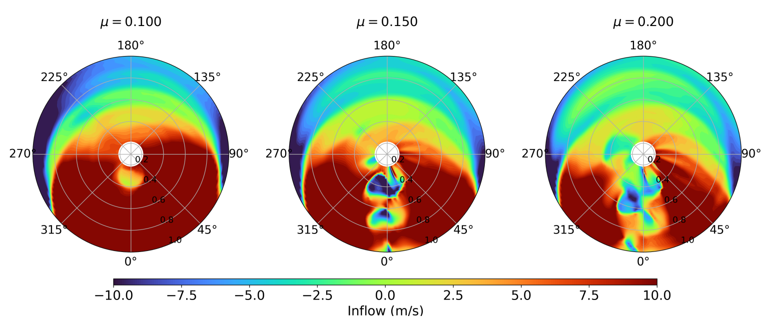

(b) $C_T/\sigma = 0.09$.

Figure 8: Contour plots of inflow velocity z component at advance ratios $\mu = 0.10$, $\mu = 0.15$, and $\mu = 0.2$.